

Diverse polarization angle swings from a repeating fast radio burst source

<https://doi.org/10.1038/s41586-020-2827-2>

Received: 21 November 2019

Accepted: 1 September 2020

Published online: 28 October 2020

 Check for updates

R. Luo^{1,2,3}, B. J. Wang^{1,2}, Y. P. Men^{1,2}, C. F. Zhang^{1,2}, J. C. Jiang^{1,2}, H. Xu^{1,2}, W. Y. Wang^{2,4}, K. J. Lee^{1,2,5}, J. L. Han^{2,4,5,6}, B. Zhang^{6,8}, R. N. Caballero¹, M. Z. Chen⁷, X. L. Chen^{2,4}, H. Q. Gan^{2,5}, Y. J. Guo^{1,8}, L. F. Hao⁹, Y. X. Huang⁹, P. Jiang^{2,5}, H. Li^{2,4}, J. Li⁷, Z. X. Li⁹, J. T. Luo¹⁰, J. Pan², X. Pei^{4,7}, L. Qian^{2,5}, J. H. Sun^{2,5}, M. Wang⁹, N. Wang⁷, Z. G. Wen⁷, R. X. Xu^{1,11}, Y. H. Xu⁹, J. Yan^{2,5}, W. M. Yan⁷, D. J. Yu^{2,5}, J. P. Yuan⁷, S. B. Zhang^{3,4,12} & Y. Zhu^{2,5}

Fast radio bursts (FRBs) are millisecond-duration radio transients^{1,2} of unknown origin. Two possible mechanisms that could generate extremely coherent emission from FRBs invoke neutron star magnetospheres^{3–5} or relativistic shocks far from the central energy source^{6–8}. Detailed polarization observations may help us to understand the emission mechanism. However, the available FRB polarization data have been perplexing, because they show a host of polarimetric properties, including either a constant polarization angle during each burst for some repeaters^{9,10} or variable polarization angles in some other apparently one-off events^{11,12}. Here we report observations of 15 bursts from FRB 180301 and find various polarization angle swings in seven of them. The diversity of the polarization angle features of these bursts is consistent with a magnetospheric origin of the radio emission, and disfavours the radiation models invoking relativistic shocks.

Thanks to its high sensitivity, the Five-hundred-meter Aperture Spherical radio Telescope (FAST)¹³ is well positioned to search for repeating bursts from FRB sources and carry out polarization observations. FRB 180301 was discovered by the Parkes 64-m radio telescope¹⁴, and has a dispersion measure (DM) of 522 cm⁻³ pc. We carried out four observations for this source in July, September and October 2019 with a total observing time of 12 h (see Extended Data Table 1) using the 19-beam receiver mounted on FAST, covering the frequency range 1,000–1,500 MHz. In the July and September sessions, the central beam (with a 3' beam size at full-width at half-maximum, FWHM) of the 19-beam receiver was pointed at the previously reported position (right ascension, $\alpha = 6\text{ h }12\text{ min }43.4\text{ s}$; declination, $\delta = +04^\circ 33' 45.4''$) from the Parkes discovery observation¹⁴ (in which the telescope's FWHM beam size was 14.1'). Four bursts were detected using Beam 7 in the July session, in which we recorded only two linear polarization intensity channels. Based on the fact that we did not detect any burst signal in beams other than Beam 7, we estimated the FRB position to be at $\alpha = 6\text{ h }12\text{ min }54.96\text{ s}$ and $\delta = +04^\circ 38' 43.6''$ with an error circle of 2.6' (see Methods). No burst above the detection threshold (signal-to-noise ratio, $S/N \geq 8$) was found in the September session. In the two sessions in October, the FAST central beam was pointed to the July position of Beam 7, and 11 more bursts were detected, with the full polarimetric data recorded. The pulse profiles and dynamic spectra of these bursts with time and frequency are presented in Extended Data Fig. 1 (see Methods). When they are dedispersed to maximize the frequency-integrated

temporal structure, these bursts have $DM \approx 517\text{ cm}^{-3}\text{ pc}$ (see Table 1). Their peak flux densities range from 5.3 mJy to 94.1 mJy.

The bursts show rich pulse structures without a common pattern. All the bursts have intrinsic widths of a few microseconds with no apparent evidence of scattering (see Table 1). These features resemble those typically seen in repeating FRBs^{10,15–17}. Some bursts (for example, burst 5) show a clear frequency down-drifting pattern, as also observed in some other repeating bursts^{10,16–18}, suggesting a common physical origin.

The bursts show a diversity of polarimetric properties. Polarization pulse profiles of seven bursts with the best S/N polarization data, together with their dynamic spectra are presented in Fig. 1. These bursts have a high degree of linear polarization, some with a degree of polarization of $I > 70\%$. On the other hand, no obvious circular polarization was detected for any of the bursts, with an upper limit of 3% for the strong bursts 5, 9, 11, 12 and 13, and of about 10% for the weak bursts 7 and 10. These properties are similar to those of some repeating FRBs, such as FRB 121102, which show a nearly 100% linear polarization and circular polarization of less than a few per cent⁹. However, FRB 180301 shows a rich diversity of polarization position angle (PA) swings across the pulse profiles—for example, sweeping up for bursts 9 and 13, sweeping down for burst 11, or up and down for burst 12—although some (for example, burst 10) are consistent with a non-varying PA during the burst. These polarization features have not been detected in previous observations, which showed, for example, a nearly constant PA during each

¹Kavli Institute for Astronomy and Astrophysics, Peking University, Beijing, China. ²National Astronomical Observatories, Chinese Academy of Sciences, Beijing, China. ³CSIRO Astronomy and Space Science, Australia Telescope National Facility, Epping, New South Wales, Australia. ⁴School of Astronomy, University of Chinese Academy of Sciences, Beijing, China. ⁵CAS Key laboratory of FAST, National Astronomical Observatories, Chinese Academy of Sciences, Beijing, China. ⁶Department of Physics and Astronomy, University of Nevada, Las Vegas, NV, USA. ⁷Xinjiang Astronomical Observatory, Chinese Academy of Sciences, Urumqi, China. ⁸Max-Planck institut für Radioastronomie, Bonn, Germany. ⁹Yunnan Observatories, Chinese Academy of Sciences, Kunming, China. ¹⁰National Time Service Center, Chinese Academy of Sciences, Xi'an, China. ¹¹State Key Laboratory of Nuclear Physics and Technology, School of Physics, Peking University, Beijing, China. ¹²Purple Mountain Observatory, Chinese Academy of Sciences, Nanjing, China. ✉e-mail: kjlee@pku.edu.cn; hjl@nao.cas.cn; zhang@physics.unlv.edu

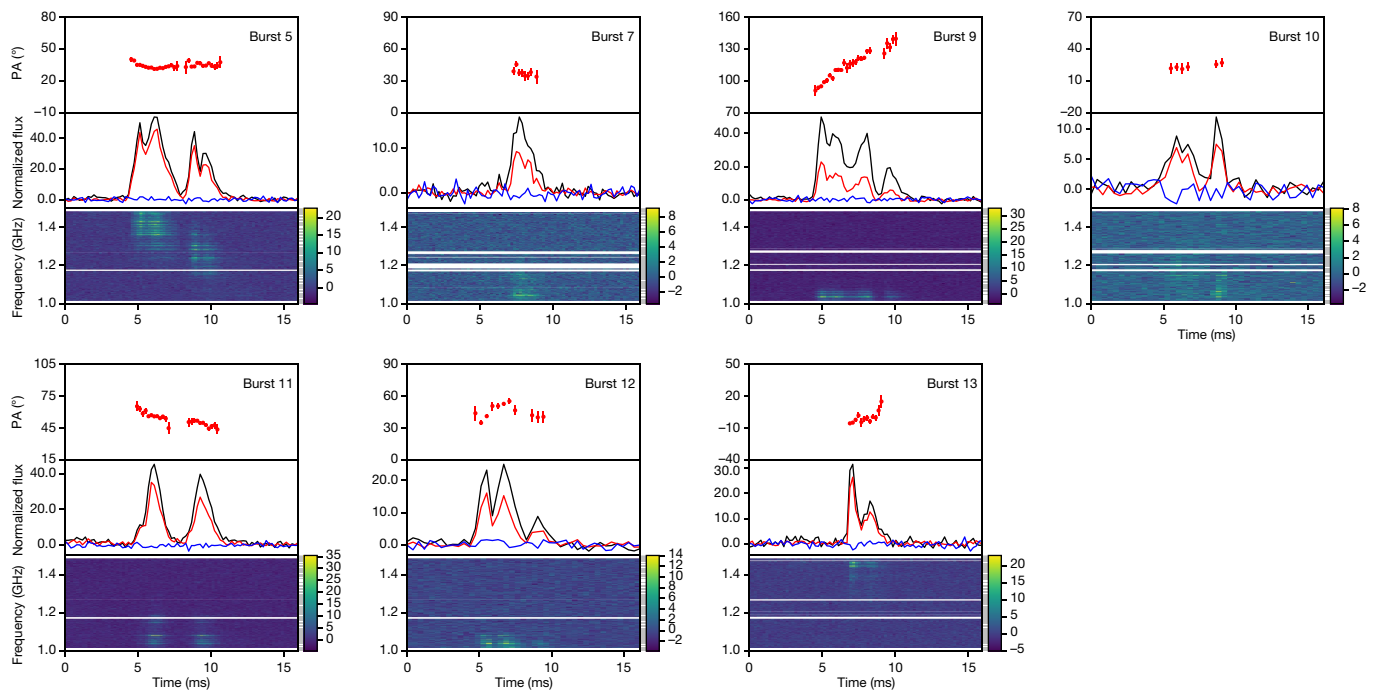


Fig. 1 | Polarization profiles and dynamic spectra of the seven brightest bursts from FRB 180301. The Bayesian RM of each burst listed in Table 1 is used to derotate the linear PA. Top, PA of linear polarization at infinite frequency; error bars represent 68% confidence. Middle, polarization pulse profile; black, red and blue curves denote total intensity, linear polarization and circular polarization, respectively. Bottom, dynamic spectra of the total intensity as a function of frequency and time (frequency resolution 1.95 MHz per channel and time resolution 196.6 μ s per bin for all bursts except bursts 10 and 12, which

are plotted with a time resolution of 393.2 μ s per bin). The colour bars denote the intensity S/N , that is, the flux scaled with the off-pulse r.m.s. amplitude. $DM_{aligned}$ in Table 1 is used to dedisperse each burst. The PA curves are plotted in the same scale with a total range of 90°. One can see a rich diversity of PA swings across the pulse profiles—for example, sweeping up for bursts 9 and 13, sweeping down for burst 11, or up and down for burst 12—even though some (for example, burst 10) are consistent with a non-varying PA during the burst.

Table 1 | Measured parameters of the bursts from FRB 180301

Burst number	Arrival time ^a (MJD)	$DM_{S/N}$ ^b (cm^{-3} pc)	$DM_{aligned}$ ^c (cm^{-3} pc)	S^d (mJy)	S/N	Width (ms)	τ_s ^e (ms)	Π^f (%)	RM_{Bayes} ^g ($rad m^{-2}$)	RM_{syn} ^h ($rad m^{-2}$)
1	58680.09189754	521.1 ± 0.1	518.3 ± 1.2	40.5	46.4	3.7 ± 0.1	<0.5	–	–	–
2	58680.11702228	522.3 ± 1.4	–	7.2	11.4	7.1 ± 0.7	–	–	–	–
3	58680.11785237	519.9 ± 0.4	–	11.5	11.5	2.8 ± 0.3	<0.1	–	–	–
4	58680.14004130	525.1 ± 1.7	–	8.6	12.9	6.3 ± 0.5	–	–	–	–
5	58762.87166882	520.7 ± 0.1	516.8 ± 1.6	94.1	155.1	4.3 ± 0.1	<1	79.5 ± 1.0	$535.2^{+0.5}_{-0.6}$	534.7 ± 2.6
6 ⁱ	58762.90818370	517.3 ± 0.7	–	10.7	14.3	2.8 ± 0.2	<6	–	–	–
7	58762.91573324	517.3 ± 0.2	516.6 ± 0.7	18.8	29.5	3.9 ± 0.1	0.1	46.9 ± 4.5	$547.5^{+2.8}_{-2.7}$	547.7 ± 3.8
8 ⁱ	58762.94422687	510.3 ± 2.3	516.6 ± 1.3	6.8	14.4	7.1 ± 0.6	<10	–	–	–
9	58762.97852743	517.1 ± 0.2	516.3 ± 2.6	60.2	120.1	6.3 ± 0.1	<4	36.6 ± 0.9	$521.0^{+4.6}_{-4.2}$	522.6 ± 8.5
10	58762.97985277	518.9 ± 0.3	517.0 ± 0.6	10.3	17.7	4.7 ± 0.3	<0.7	67.4 ± 7.0	$542.6^{+2.7}_{-2.6}$	557.2 ± 8.8
11	58763.86585273	517.1 ± 0.1	516.6 ± 0.8	43.2	88.9	6.7 ± 0.9	<0.2	69.0 ± 1.4	$555.7^{+0.9}_{-0.9}$	559.4 ± 2.8
12	58763.86585290	516.9 ± 0.4	515.9 ± 2.3	21.2	39.5	5.5 ± 0.2	<4	55.6 ± 2.9	$552.8^{+6.4}_{-4.4}$	548.7 ± 7.1
13	58763.88351268	516.9 ± 0.2	516.7 ± 1.7	32.5	45.5	3.1 ± 0.1	<10	73.6 ± 3.2	$563.9^{+3.4}_{-4.0}$	552.7 ± 13.4
14 ⁱ	58763.92197253	522.7 ± 1.4	–	7.1	17.7	9.8 ± 0.6	–	–	–	–
15 ⁱ	58763.97110374	525.5 ± 0.6	–	5.3	9.8	5.5 ± 0.6	–	–	–	–

^aInfinite-frequency arrival times at the Solar System barycentre.

^bDM obtained by maximizing S/N .

^cDM obtained by the best burst alignment.

^dPeak flux density. Uncertainties are dominated by the variation of the system noise temperature (~20%)²³.

^eScattering timescale at 1 GHz at 68% confidence level, determined by curve fitting²⁶.

^fDegree of polarization.

^gRM at 68% confidence level, obtained by the Bayesian method.

^hRM at 68% confidence level, obtained by RM synthesis.

ⁱBecause of the the low S/N (≤ 5), we neglect the degree of polarization for bursts 6, 8, 14 and 15.

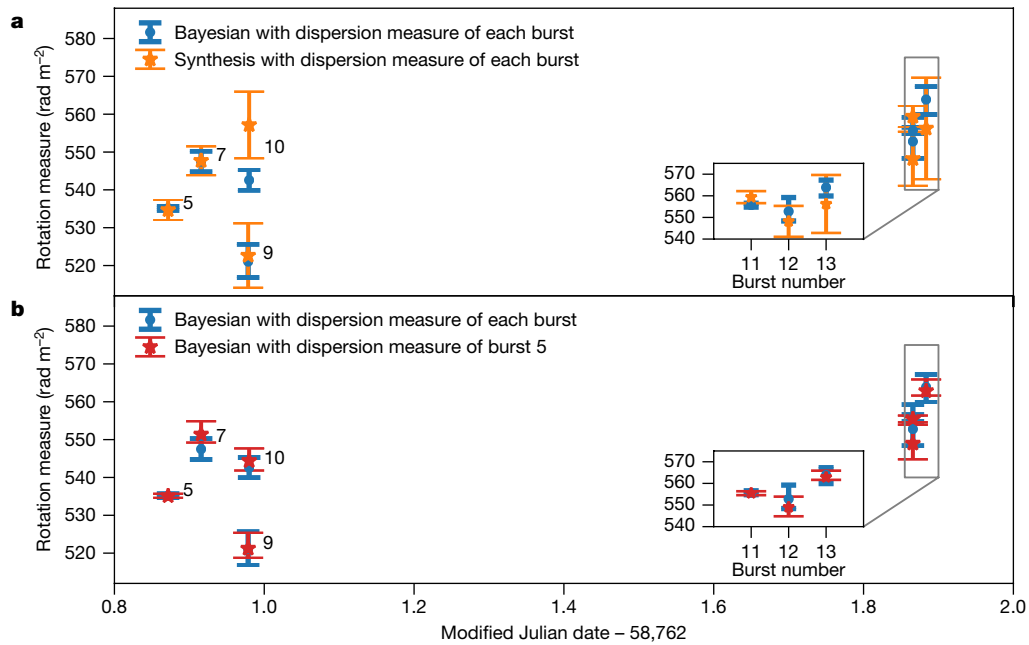


Fig. 2 | RM values of seven bursts from FRB 180301. a, Comparison between RM values measured with the Bayesian and with the RM synthesis method. The burst numbers are defined in Table 1. The error bars denote the 68% confidence intervals. Blue points denote RMs computed using the Bayesian method with

the DM_{align} values in Table 1; orange stars represent RM values computed with the RM synthesis method. **b**, Comparison between RMs calculated using DM_{align} (blue points) and the DM of burst 5 (red stars). The details of RM inference are given in Methods.

burst from repeaters such as FRB 121102⁹ and FRB 180916.J0158+65¹⁰, PA swings for some apparently non-repeating FRBs^{11,12}, or a considerable amount of circular polarization from some FRBs¹⁹. Our observations revealed a high level of diversity for the PA swings of repeating bursts from one source, suggesting that polarimetric properties are not a good indication for distinguishing repeaters from apparent non-repeaters.

The detection of linear polarization allowed the measurement of the Faraday rotation measure (RM; see details in Methods). For seven bursts with polarization data recorded and $S/N > 5$ for the polarization intensity, we calibrated the data and found similar RM values ranging from $521.5^{+4.6}_{-4.2}$ rad m⁻² to $564.4^{+3.4}_{-4.0}$ rad m⁻² (68% confidence level), very different from that reported ($-3,163 \pm 20$ rad m⁻²) in the initial discovery¹⁴. It is possible that the previous reported RM value was biased owing to the narrow signal bandwidth of 40 MHz (see Methods). RM variations on a wide range of timescales have been reported for FRB 121102⁹, including a variation of about 0.5% (~ 500 rad m⁻²) over a month and of 10% ($\sim 10^4$ rad m⁻²) over seven months. A small burst-to-burst RM change for FRB 121102 (~ 50 rad m⁻²) cannot be ruled out. For FRB 180301, a χ^2 test (see Methods) shows that the RM is unlikely to be a constant, varying on a timescale of one day, as shown in Fig. 2. Such an RM variation is not affected by the DM uncertainties, because the results are nearly the same when using either the DM values inferred from each burst or the DM of the burst with the highest S/N (burst 5). Our measured RM values have a possible linear trend with a slope of 21 rad m⁻² d⁻¹ and pulse-to-pulse RM variations with a root-mean-square (r.m.s.) amplitude of 14 rad m⁻².

FRB models typically address both the source of the burst and the radiation mechanism. The polarization dataset presented here offers clues in understanding the radiation mechanisms of repeating FRBs. Two groups of radiation models have been widely used to interpret the extremely high brightness temperatures of FRBs. One group of models invokes a magnetosphere of a neutron star to radiate coherent emission^{3,5}, whereas the other group invokes the synchrotron maser mechanism in relativistic shocks from a highly magnetized neutron star^{7,8}. Both groups of models are able to interpret strong linear polarization with non-varying PAs, as observed in FRB 121102 and FRB 180916.J0158+65. The magnetospheric models invoke ordered field lines that

sweep the line of sight as the source rotates²⁰ (as frequently observed in radio pulsars and flaring magnetars^{21–23}) or as the magnetospheric configuration is reshaped by an external ram pressure⁴. Depending on the magnetospheric configuration and line-of-sight geometry, the magnetosphere models can produce diverse PA swing patterns (including a non-varying PA pattern²⁴). However, the synchrotron maser models require the ordered magnetic field in the shock plane to reach the coherent condition for radio emission. These models predict a constant PA during each pulse^{7,8} and have great difficulties in producing diverse PA variation patterns across pulses. The observations reported here therefore disfavour the synchrotron maser mechanism but support a magnetospheric origin of FRB radio emission (Methods).

The burst rate of FRB 180301 is $1.2^{+0.8}_{-0.7}$ h⁻¹ with a shape parameter of $k = 0.9 \pm 0.3$ (see Methods) assuming a Weibull distribution²⁵, when we count 15 bursts detected by FAST in the four sessions with a flux density threshold of 5 mJy. The shape parameter is close to 1, which suggests that the burst arrival times can be well described by a Poissonian distribution. The high burst rate makes FRB 180301 an active repeater, similar to FRB 121102. FRB 121102⁹ has an exceptionally large RM value, which has been interpreted as either due to a putative special location close to a supermassive black hole^{9,24} or due to a strong magnetic field in the wind or supernova remnant of a very young magnetar⁷. Within the magnetar scenario, if the burst rate is a proxy for the age of the underlying magnetar, other factors are needed to account for the RM discrepancy between FRB 180301 and FRB 121102.

Online content

Any methods, additional references, Nature Research reporting summaries, source data, extended data, supplementary information, acknowledgements, peer review information; details of author contributions and competing interests; and statements of data and code availability are available at <https://doi.org/10.1038/s41586-020-2827-2>.

1. Lorimer, D. R., Bailes, M., McLaughlin, M. A., Narkevic, D. J. & Crawford, F. A bright millisecond radio burst of extragalactic origin. *Science* **318**, 777–780 (2007).
2. Petroff, E., Hessels, J. W. T. & Lorimer, D. R. Fast radio bursts. *Astron. Astrophys. Rev.* **27**, 4 (2019).

3. Kumar, P., Lu, W. & Bhattacharya, M. Fast radio burst source properties and curvature radiation model. *Mon. Not. R. Astron. Soc.* **468**, 2726–2739 (2017).
4. Zhang, B. A. “Cosmic comb” model of fast radio bursts. *Astrophys. J. Lett.* **836**, 32 (2017).
5. Yang, Y.-P. & Zhang, B. Bunching coherent curvature radiation in three-dimensional magnetic field geometry: application to pulsars and fast radio bursts. *Astrophys. J.* **868**, 31 (2018).
6. Lyubarsky, Y. A model for fast extragalactic radio bursts. *Mon. Not. R. Astron. Soc.* **442**, L9–L13 (2014).
7. Metzger, B. D., Margalit, B. & Sironi, L. Fast radio bursts as synchrotron maser emission from decelerating relativistic blast waves. *Mon. Not. R. Astron. Soc.* **485**, 4091–4106 (2019).
8. Beloborodov, A. M. Blast waves from magnetar flares and fast radio bursts. *Astrophys. J.* **896**, 142 (2020).
9. Michilli, D. et al. An extreme magneto-ionic environment associated with the fast radio burst source FRB 121102. *Nature* **553**, 182–185 (2018).
10. CHIME/FRB Collaboration et al. CHIME/FRB discovery of eight new repeating fast radio burst sources. *Astrophys. J. Lett.* **885**, 24 (2019).
11. Masui, K. et al. Dense magnetized plasma associated with a fast radio burst. *Nature* **528**, 523–525 (2015).
12. Cho, H. et al. Spectropolarimetric analysis of FRB 181112 at microsecond resolution: implications for fast radio burst emission mechanism. *Astrophys. J. Lett.* **891**, 38 (2020).
13. Jiang, P. et al. Commissioning progress of the FAST. *Sci. China Phys. Mech. Astron.* **62**, 959502 (2019).
14. Price, D. C. et al. A fast radio burst with frequency-dependent polarization detected during Breakthrough Listen observations. *Mon. Not. R. Astron. Soc.* **486**, 3636–3646 (2019).
15. Spitler, L. G. et al. A repeating fast radio burst. *Nature* **531**, 202–205 (2016).
16. CHIME/FRB Collaboration A second source of repeating fast radio bursts. *Nature* **566**, 235–238 (2019).
17. Fonseca, E. et al. Nine new repeating fast radio burst sources from CHIME/FRB. *Astrophys. J. Lett.* **891**, 6 (2020).
18. Hessels, J. W. T. et al. FRB 121102 bursts show complex time-frequency structure. *Astrophys. J. Lett.* **876**, 23 (2019).
19. Petroff, E. et al. A polarized fast radio burst at low Galactic latitude. *Mon. Not. R. Astron. Soc.* **469**, 4465–4482 (2017).
20. Radhakrishnan, V. & Cooke, D. J. Magnetic poles and the polarization structure of pulsar radiation. *Astrophys. J.* **3**, 225–229 (1969).
21. Levin, L. et al. Radio emission evolution, polarimetry and multifrequency single pulse analysis of the radio magnetar PSR J1622–4950. *Mon. Not. R. Astron. Soc.* **422**, 2489–2500 (2012).
22. Eatough, R. P. et al. A strong magnetic field around the supermassive black hole at the centre of the Galaxy. *Nature* **501**, 391–394 (2013).
23. Camilo, F. et al. Radio disappearance of the magnetar XTE J1810–197 and continued X-ray timing. *Astrophys. J.* **820**, 110 (2016).
24. Zhang, B. FRB 121102: a repeatedly combed neutron star by a nearby low-luminosity accreting supermassive black hole. *Astrophys. J. Lett.* **854**, 21 (2018).
25. Oppermann, N., Yu, H.-R. & Pen, U.-L. On the non-Poissonian repetition pattern of FRB121102. *Mon. Not. R. Astron. Soc.* **475**, 5109–5115 (2018).
26. Spitler, L. G. et al. Pulse broadening measurements from the Galactic Center pulsar J1745–2900. *Astrophys. J. Lett.* **780**, 3 (2013).

Publisher's note Springer Nature remains neutral with regard to jurisdictional claims in published maps and institutional affiliations.

© The Author(s), under exclusive licence to Springer Nature Limited 2020

Methods

Observations and burst detection

The observations were carried out using the FAST telescope, which has an effective collecting area of 300 m in diameter, mounted with the 19-beam receiver. The system temperature is about 20–25 K for different beams, as reported in the specifications of the FAST L-band system²⁷. The designed frequency response of the 19-beam receiver covers 1,050–1,450 MHz with the central frequency at 1,250 MHz; in reality, signals of 1,000–1,500 MHz with a degraded bandpass of 50 MHz at each of the two edges are also received and down-converted. The raw voltages were digitized using a pulsar backend based on the Re-configurable Open Architecture Computing Hardware-2 (ROACH2) system²⁸, where the voltage data are correlated and integrated to form filterbank data with a time resolution of 49.152 μ s. The entire 500-MHz bandwidth is divided into 4,096 channels. As a search observation, two orthogonal linear polarization intensity channels were recorded.

Observations were carried out in four sessions (see Extended Data Table 1). During the first session on 16 July 2019, we detected four bursts over a 2-h observation, and the burst signal was seen only in Beam 7 (out of 19 beams). Later in the same year, 4-, 3- and 3-h follow-up observations were carried out on 11 September, 6 October and 7 October, respectively. No burst was detected in the second session, but six and five bursts with full-polarization Stokes parameters were recorded in the third and fourth sessions when the central beam of the receiver was placed on the new position (see below).

We used the BEAR (Burst Emission Automatic Roger) package²⁹ to perform the FRB searches. BEAR is capable of performing radio-frequency interference (RFI) mitigation, dedispersion and candidate score ranking in one run. When searching for bursts, data at 1,200–1,250 MHz were excluded to avoid satellite interference. We dedispersed the data with DM trials in 500–550 cm^{-3} pc in steps of 0.5 cm^{-3} pc. To reduce the computational cost, the pulse width was searched from 0.2 ms to 20 ms in the box-car-shaped matched filter of BEAR. The signals were then sifted visually for candidates with $S/N > 8$. The RFI at the FAST site is dominated only by satellite signals thanks to the radio protection zone. The narrow-band, close-to-zero DM signals were classified as RFI. Although we searched only with a DM range of 500–550 cm^{-3} pc, the zero-DM time series was always computed by the RFI filter of BEAR. Signals with a strong indication of cold-plasma dispersion were recorded as FRB candidates. We also plotted all the candidates using a graphical interface, where RFI and FRB signals can be well separated in the DM and S/N space. The dynamic spectra of all 15 bursts detected are presented in Extended Data Fig. 1.

Localization and position accuracy

All the 19 beams had an average full half-power beam width (HPBW) of 3' and were spaced by 5.74' in a cellular structure²⁷. Because burst 5—the strongest one that we detected, with $S/N = 155$ —was not detected in the six beams surrounding the central beam above the S/N threshold of 8, the angular distance of FRB 180301 from the centre of Beam 1 cannot be larger than $\sim 2.6'$. Otherwise, it would appear in the sidelobes of other beams. The pointing error of FAST is less than 15", which is much smaller than the HPBW. We therefore conclude that the position of this FRB is located at $\alpha = 6 \text{ h } 12 \text{ min } 54.96 \text{ s}$ and $\delta = +04^\circ 38' 43.6''$ with a position uncertainty of 2.6' (radius, 68% confidence level).

Dispersion measure

DM values obtained by aligning the signal across frequencies to achieve the best peak S/N (ref.³⁰) or by maximizing the temporal structure will be different¹⁸. Here we report both kinds of DM values (Table 1). Deriving the DM from the maximization of S/N has been well documented³⁰. To maximize the temporal structure, we maximize the S/N -weighted 'local contrast' of the dedispersed pulse profile, as

defined in equation (1). Previously, this was done without the S/N weight¹⁸. The estimated $\widehat{\text{DM}}$ is

$$\widehat{\text{DM}} = \arg\max_{\text{DM}} \max \left\{ \frac{[s(\text{DM})_i - s(\text{DM})_{i-1}]^2}{s(\text{DM})_i + s(\text{DM})_{i-1}} \left[\frac{s(\text{DM})_i + s(\text{DM})_{i-1}}{\sigma} \right]^2 \right\} \quad (1)$$

$$\forall i \in [2, N]$$

for N data points in the dedispersed pulse profile (s). We use the r.m.s. value of the integrated profile baseline to estimate the profile error (σ). The first term in the equation is the local contrast, that is, the ratio between the difference of the i th bin and the $(i-1)$ th bin ($s_i - s_{i-1}$) and their mean. The second term is the S/N weight. In practice, we dedisperse the dynamic spectra in a series of DM trials to get the profiles. Then, we calculate the maximum of the local contrast of each profile to get the best alignment of the pulses. The optimal DM is $\text{DM}_{\text{aligned}}$ in Table 1. The DM error is determined by the FWHM of the contrast–DM curve. This approach gives a better determined DM (weighted mean DM = 516.76 cm^{-3} pc with standard deviation of $\Delta(\text{DM}) = 0.62 \text{ cm}^{-3}$ pc) compared to the previously used method¹⁸ (weighted mean DM = 516.23 cm^{-3} pc with standard deviation of $\Delta(\text{DM}) = 1.19 \text{ cm}^{-3}$ pc), because the S/N weighting in our method helps to reduce the uncertainty.

Redshift inference

The redshift of FRB 180301 is inferred using the method described by Luo et al.³¹, in which the cosmic co-moving volume size is used as the distance prior and galaxy synthesis is applied to determine the likelihood function of the observed DM with a certain redshift z . The extragalactic DM was obtained by removing the foreground contribution from the Milky Way using both the NE2001³² and the YMW16³³ models. We used the DM from the halo with the mean value $\text{DM}_{\text{halo}} \approx 30 \text{ cm}^{-3}$ pc from the simulation³⁴, and the relation $\text{DM}_{\text{IGM}} - z$ using the standard formula³⁵ with intergalactic medium fraction $f_{\text{IGM}} \approx 0.83$. We inferred the redshift using the maximal posterior inference. According to the galaxy synthesis model³¹, the redshift range at 95% confidence level is $z = 0.20\text{--}0.35$ using the NE2001 model and $z = 0.13\text{--}0.23$ using the YMW16 model.

Polarization and Faraday rotation

We performed the polarization calibration with the PSRCHIVE³⁶ software package (<http://psrchive.sourceforge.net>) using the single-axis model, in which the differential gain and phase are calibrated using the noise diode. Such a calibration scheme can reduce the systematics down to the 0.5% level, as the leakage term is better than -46 dB within the FWHM region of the central beam as measured in the FAST engineering phase³⁷. The polarization data were recorded at 1,000–1,500 MHz. The feed efficiency drops below 70% and the noise temperature rises steeply³⁷ near the band edge; therefore, we only used data in the range 1,020–1,480 MHz for later analysis. We checked the bandpass of Stokes intensity parameter V in the pulse region, as shown in Fig. 1. The fluctuation is compatible with the r.m.s. amplitude in the off-pulse region, which indicates that the differential phase between the two linear feeds was calibrated properly.

Among the 11 bursts detected in the third and fourth observations, seven have high S/N for the polarization intensity ($S/N_{\text{pol}} \geq 5$), with which the Faraday rotation can be measured. Frequency channels containing strong RFI were excluded, as marked in Extended Data Fig. 2. The bins with integrated $S/N < 5$ were also excluded.

There are two major classes of methods with which to measure the RM: (1) Q – U fitting, which fits the Stokes intensity parameters Q and U using sinusoidal curves³⁸; and (2) RM synthesis³⁹, which derotates the RM-induced PA wrap and uses the maximum of the total linear polarization to determine the RM. The two methods are complementary because the Q – U fitting method has a solid statistical foundation

in parameter inference, whereas the RM synthesis method provides a global view of the linear polarization intensity as a function of the wide RM range⁴⁰. As a parameter estimation problem, it is preferable to use $Q-U$ fitting with Bayesian inferences³⁸ as the primary method to measure the Faraday rotation in the observer frame. Nevertheless, we compare the result obtained using this method with that obtained using the RM synthesis method³⁹ to cross-check the measured RM values and to make sure that the inferred parameters do not fall into a local minimum.

The Bayesian method³⁸ includes modelling the systematics and deviation of RM-induced linear polarization wrapping, so it generally produces reliable RM values. The Stokes parameters Q and U are integrated in the burst time intervals, binned to a frequency resolution of 1.95 MHz per channel. As shown in Extended Data Fig. 2, we detected clear RM features for each burst, that is, the sinusoidal curves of the Stokes parameters Q and U as functions of wavelength. After the RM measurement, we used the software package IONFR⁴¹ to compute the ionospheric corrections, with values below 1 rad m⁻². The corrected RM values are listed in Table 1.

We cross-checked the RM values using the ‘revisited’ RM synthesis³⁹. The polarization dynamic spectra were normalized by the baseline r.m.s. value of the total intensity in each channel. Then, the Stokes parameters Q and U were derotated with trial RM values ranging from $-8,000$ rad m⁻² to $+8,000$ rad m⁻², a range chosen to cover much more than the original RM of $-3,163 \pm 20$ rad m⁻² given in the initial discovery¹⁴. Here, the ‘revisited’ derotation vector was used to correct the systematics caused by uniform frequency sampling, as explained in ref.³⁹. The degree of linear polarization for each trial RM was then calculated from the linearly polarized profile and the total intensity profile. Following the convention³⁶, the uncertainty of the RM values was estimated using half of the FWHM divided by the S/N value of the local Gaussian peak. The RM spectra are shown in Extended Data Fig. 3. The measured RM values are compared with the Bayesian values in Table 1 and Fig. 2a.

We checked whether the RM value or polarization profile could be affected by the value of DM used in the dedispersion by comparing the measured RM values produced by a different data-processing pipeline, in which we fixed the DM for all bursts. We chose to fix the DM to the value of burst 5, which has the widest bandwidth and the highest S/N among all bursts. The measured RM values for aligned/fixed-DM sets agree with each other within the uncertainties.

To make sure that the RM measurement was not affected by the polarimetry instability of FAST or off-axis illumination, we conducted three extra test observations with a pulsar, PSR J1915+1009, on 16 and 17 January 2020. The DM and RM values of PSR J1915+1009 are similar to those of FRB 180301, and its position is known accurately. In the first test observation, the pulsar was placed at the centre of the central beam; in the second test observation, the pulsar was placed 2.6′ (see Methods section ‘Localization and position accuracy’) away from the beam centre; and the third test observation was conducted one day later with the pulsar at the beam centre. We checked the temporal stability of the Bayesian RM measurement using the first and third test observations. As shown in Extended Data Fig. 4a, no RM variation is found in the test pulsar observation. The maximum RM variation is 0.1 rad m⁻² over the two-day timescale. We examined the off-axial polarization error by comparing the RM measured in the first and second observation sessions. As shown in Extended Data Fig. 4b, the maximum difference is 0.3 rad m⁻². We also checked the linear and circular degrees of polarization by comparing the pulse profiles of the three observation sessions carried out at FAST with previously published results⁴². As one can see in Extended Data Fig. 4c–e, both linear and circular polarizations are stable. Therefore, the RM values that we measured for FRB 180301 are not affected by instrumental instability.

Our RM values are highly different from that reported ($-3,163 \pm 20$ rad m⁻²) in the initial discovery¹⁴, in which the signal was bright only in a 40-MHz frequency window and the so-produced linear

polarization in the integrated profile was not apparent. Although it is possible that the RM value changed so dramatically owing to the compact magnetoionic environment, such a discrepancy in RM values probably comes from the narrow-band bias of the RM transfer function⁴³, that is, the previously reported value may be biased because of the just 40 MHz effective bandwidth. With the RM values that we obtained, the degree of linear polarization for the RM-corrected pulse profile is rather high (36–80%).

Such a high RM of -550 rad m⁻² cannot be easily explained by the Galactic foreground, which is measured to be $+72 \pm 8$ rad m⁻² at these Galactic coordinates, according to Xu & Han⁴⁴ (see also the <http://zmt.bao.ac.cn/RM/searchGRM.html>). Likewise, the intergalactic RM contribution⁴⁵ is estimated to be at most a few to a few tens of radians per square metre. The remaining observed RM is contributed by the host galaxy or local environment at redshift $z \approx 0.13-0.35$, which implies that the intrinsic RM in the source rest frame is $(RM_{\text{obs}} - RM_{\text{Gal}}) \times (1+z)^2 = (550 - 72) \times (1.27 \text{ to } 1.82) \approx 600$ to 870 rad m⁻². The most probable origin of this large RM is from the local environment—as opposed to the interstellar medium of the host galaxy.

As one can see, the RM values measured with the Bayesian and the RM synthesis methods are consistent. For six out of seven measurements, the results of the two methods agree within 1σ , and all seven measurements agree within 2σ . Because the two methods belong to different classes of statistics, their errors have different meanings. Nevertheless, we note that the RM synthesis tends to produce larger errors than the Bayesian method. We also combine the RM synthesis spectra of different bursts to fit the RM values jointly. The combined RM spectra are shown in Extended Data Fig. 5. The jointly fitted RM values are 535.8 ± 2.7 rad m⁻² on 6 October 2019 (bursts 5, 7, 9, 10), 558.9 ± 3.7 rad m⁻² on 7 October 2019 (bursts 11, 12, 13) and 543.7 ± 2.6 rad m⁻² for all seven bursts. The three joint-fitting results indicate an RM variation. Using the Bayesian RM values in Table 1, the computed χ^2 becomes $\chi^2 = 450$ (corresponding to 21σ). If we use the RM synthesis values, $\chi^2 = 51 \times 6\sigma$. The RM values for data dedispersed with the DM of burst 5 produce a similar level of χ^2 , and the conclusion does not change. The χ^2 test indicates that the RM is probably not a constant.

We investigated whether the RM changes during the bursts but found no such variation. Phase-resolved RM variation has been reported for radio pulsars⁴⁶ and for FRB 181112¹². As shown by Noutsos et al.⁴⁶, the phase-dependent RM variation may come from scattering in interstellar ionized medium or from propagation effects in the magnetosphere. Cho et al.¹² noted that the RM differs by approximately 25 rad m⁻² within one burst from FRB 181112. Here, the null detection of phase-dependent RM variation in FRB 180301 could be a consequence of the limited S/N . However, it is also possible that the scattering effect of FRB 180301 is too weak to produce RM variation during the burst.

We checked whether the measured RM spectra are consistent with the thin-screen model. Data of burst 5 were used for the test because it has the best S/N . As shown in Extended Data Fig. 6, after we subtract the linear polarization contribution of the best-fitted RM (that is, the spectrum of a thin Faraday screen), the remaining RM spectrum is consistent with noise, suggesting that the radiation comes from a compact region with the same Faraday depth.

Polarization angles of bursts

After correcting for the RM, we have the infinite-frequency polarization profile of each burst. The RM-corrected profiles with the individual Bayesian RM values are shown in Fig. 1. For the diverse PA swings observed from FRB 180301, even though bursts 5, 9, 11 and 13 may be characterized as pulsar-like shapes, it is unlikely that a simple rotating-vector model invoking a dipolar magnetic field²⁰ can reproduce the properties of all the bursts.

We note that there are obvious differences between the centroids of the PAs, if we derotate the linear polarization with a globally fitted RM (as shown in Extended Data Fig. 7). If we derotate the linear

polarization with the individual RM values shown in Table 1, we can approximately bring the centroids of the PAs to a constant value after taking the RM errors into account. Thus, either there is RM variation in FRB 180301 or the central values of PA swings vary pulse to pulse. During the derotation of the linear polarization with different RMs, the PA swing of each burst keeps its shape, as seen from comparing Extended Data Fig. 7 and Fig. 1.

The shape of the PA swing may depend on the DM. For example, if the DM value is inaccurate, the polarization features will be smeared and the PA swing will be flatter. To test whether the diversity of PA swing in Fig. 1 is affected by DM, we compare it with the PA swings produced using the maximum, minimum and burst-5 DM values. The polarization profiles for all cases are presented in Extended Data Fig. 8. There is little change in the shape of PA for all the bursts, even though bursts 7, 10 and 12 have a relative shift in the PA centroid. Because every 3 rad m^{-2} of RM change leads to approximately 20° of parallel shift in PA for the central frequency at 1,250 MHz, the PA shifts for bursts 7, 10 and 12 are due to a sub-error change of the RM values, as discussed in Methods section ‘Polarization and Faraday rotation’.

Coherent radiation models

The extremely high brightness temperatures observed in FRBs require that the radiation mechanism be coherent. In the literature, two broad classes of models⁴⁷ have been discussed: pulsar-like models invoking magnetospheres^{3–5,48} and γ -ray-burst-like models^{6,49,50} considering relativistic shocks. The latter invoke synchrotron masers as the coherent mechanism to emit FRBs. There are two sub-types of synchrotron maser models. One type⁴⁹ considers a non-magnetized shock, so that emission is not expected to be highly polarized. The other type^{6–8,50} invokes highly ordered magnetic fields in the shock plane to allow particles to emit coherently; to achieve this, this model requires that the magnetic field lines in the upstream medium are highly ordered. As a result, such a model predicts a constant PA across a single burst^{7,8}. To account for variation of PA across a burst, this model needs to introduce a variation of the magnetic field configuration as a function of radius in the upstream medium through which the shock propagates. A striped wind from a rotating pulsar may in principle provide a varying magnetic field configuration in the shock upstream as a function of radius⁵¹. However, this model can only generate monotonic, smoothly varying PA curves and may not account for the diverse PA evolution patterns presented in Fig. 2, such as non-monotonic variations (for example, bursts 7 and 12) and jumps in PA between sub-pulses (for example, bursts 10, 11 and 13). More complicated upstream magnetic field configurations may be possible if the medium has undergone violent disturbance due to a previous shock. However, in this case, the fields are no longer ordered, and the maser mechanism cannot operate. On the other hand, diverse PA variation features have been frequently observed in radio pulsars and flaring magnetars, the radio emission of which is believed to originate from the magnetosphere of a neutron star^{23,52}.

Magnetospheric models attribute PA variations to line-of-sight sweeping across the radiation beam. These models include the standard scenario involving neutron star rotation (as is the case of radio pulsars and flaring magnetars)^{20,52} and a scenario invoking sudden reconfiguration of a magnetosphere triggered by an external ram pressure⁴. Propagation effects—either inside the magnetosphere or far from the source, outside the magnetosphere—may provide additional mechanisms to introduce PA variation. However, these effects tend to introduce a systematic effect on all the bursts, unless the environments (for example, plasma lensing) vary rapidly within timescales of hours, which is unlikely⁵³. The fact that the PA variation patterns differ for different bursts of FRB 180301 suggests that propagation effects do not play the dominant role in shaping the PA variation patterns. Whether or not a PA variation is observed and how PA varies with time depend on the magnetic field configuration and the line-of-sight geometry. For example, the simple rotating-vector model for a dipolar magnetic

field configuration predicts an ‘S’ or ‘inverse S’ shape in the PA variation curves. More complex magnetic field configurations can produce more complicated PA variation curves. Nearly straight magnetic field lines sweeping the line of sight can produce non-varying PA patterns. This may be realized either in a rotating neutron star model with the emission region in the outer magnetosphere, or in the interaction model. The diverse PA swings observed from FRB 180301 and the failure of the simple dipolar rotating-vector model²⁰ suggest that the system may have complicated magnetic field configurations and line-of-sight geometries, which may vary with time. Such a scenario may be achieved in interacting models⁵⁴ rather than simple rotating models. This is also consistent with the lack of strict periodicity observed in repeating bursts⁵⁵. Within the magnetospheric model, the fact that many FRB bursts (including those from other sources, such as FRB 121102⁹ and FRB 180916.J0158+65¹⁰) showed a nearly constant PA during each burst would suggest that their emission region is in the outer part of the magnetosphere, where the field lines are nearly straight.

Both FRB 180301 (with varying PA) and FRB 121102 (with non-varying PA) show similar emission properties, such as complex pulse profiles¹⁵ and downward-frequency-drifting sub-pulses¹⁸. These features can be understood within a generic magnetospheric model using open-field-line regions as the FRB emission site^{56,57}. As the emission unit moves away along the open-field-line regions (either for the polar-cap geometry or the cosmic-comb geometry), an observer always sees higher-frequency emission earlier than lower-frequency emission⁵⁶.

Burst rate

Using the Kolmogorov–Smirnov test, we compare the Weibull, Gaussian and exponential distributions and find that the one that best describes the burst waiting time is the Weibull function²⁵. The p values for each case are 0.728, 0.004 and 0.202, respectively, so we can use either the Weibull or the exponential distribution to describe the waiting times. Here we adopt a Weibull distribution because the inference of its shape parameter can help to understand if there is deviation from a Poisson process.

The likelihood function of the waiting time series ΔT —that is, its probability density function—is

$$\mathcal{W}(\Delta T|k, r) = \frac{k}{\Delta T} \left[r \Delta T \Gamma \left(1 + \frac{1}{k} \right) \right]^k e^{-\left[r \Delta T \Gamma \left(1 + \frac{1}{k} \right) \right]^k}, \quad (2)$$

with the Γ function defined as $\Gamma(x) = \int_0^\infty t^{x-1} e^{-t} dt$. Here, r is the burst rate and k is the shape parameter. With the above likelihood function and assuming uniform priors, we carried out a Bayesian inference using the nested sampling software package MULTINEST⁵⁸. According to the data from all the observational sessions listed in Table 1 and the peak flux density threshold of FAST at $\sim 5 \text{ mJy}$ (see Table 1), the parameters are inferred as $r = 1.2^{+0.8}_{-0.7} \text{ h}^{-1}$ and $k = 0.9^{+0.3}_{-0.3}$ with a 95% confidence level. The posterior is plotted in Extended Data Fig. 9. The shape parameter is close to 1, which suggests that the distribution can also be well described by a Poisson process.

Data availability

The data that support the findings of this study are available at <https://psr.pku.edu.cn/index.php/publications/frb180301/>.

Code availability

The BEAR package is available at <https://psr.pku.edu.cn/index.php/publications/frb180301/>.

27. Jiang, P. et al. The fundamental performance of FAST with 19-beam receiver at L band. *Res. Astron. Astrophys.* **20**, 064 (2020).

28. Hickish, J. et al. A decade of developing radio-astronomy instrumentation using casper open-source technology. *J. Astron. Instrum.* **5**, 1641001–1641012 (2016).

29. Men, Y. P. et al. Piggyback search for fast radio bursts using Nanshan 26 m and Kunming 40 m radio telescopes – I. Observing and data analysis systems, discovery of a mysterious peryton. *Mon. Not. R. Astron. Soc.* **488**, 3957–3971 (2019).
30. Lorimer, D. R. & Kramer, M. *Handbook of Pulsar Astronomy* (Cambridge Univ. Press, 2012).
31. Luo, R., Lee, K., Lorimer, D. R. & Zhang, B. On the normalized FRB luminosity function. *Mon. Not. R. Astron. Soc.* **481**, 2320–2337 (2018).
32. Cordes, J. M. & Lazio, T. J. W. NE2001.I. A new model for the Galactic distribution of free electrons and its fluctuations. Preprint at <https://arxiv.org/abs/astro-ph/0207156> (2002).
33. Yao, J. M., Manchester, R. N. & Wang, N. A new electron-density model for estimation of pulsar and FRB distances. *Astrophys. J.* **835**, 29 (2017).
34. Dolag, K., Gaensler, B. M., Beck, A. M. & Beck, M. C. Constraints on the distribution and energetics of fast radio bursts using cosmological hydrodynamic simulations. *Mon. Not. R. Astron. Soc.* **451**, 4277–4289 (2015).
35. Deng, W. & Zhang, B. Cosmological implications of fast radio burst/gamma-ray burst associations. *Astrophys. J. Lett.* **783**, 35 (2014).
36. Hotan, A. W., van Straten, W. & Manchester, R. N. PSRCHIVE and PSRFITS: an open approach to radio pulsar data storage and analysis. *Publ. Astron. Soc. Aust.* **21**, 302–309 (2004).
37. Dunning, A. et al. Design and laboratory testing of the five hundred meter aperture spherical telescope (FAST) 19 beam L-band receiver. In *XXXIInd International Union of Radio Science General Assembly and Scientific Symposium* (eds Arnold, V. et al.), J9–1 (2017).
38. Desvignes, G. et al. Radio emission from a pulsar's magnetic pole revealed by general relativity. *Science* **365**, 1013–1017 (2019).
39. Schnitzeler, D. H. F. M. & Lee, K. J. Rotation measure synthesis revisited. *Mon. Not. R. Astron. Soc.* **447**, L26–L30 (2015).
40. Schnitzeler, D. H. F. M. & Lee, K. J. Finding a faint polarized signal in wide-band radio data. *Mon. Not. R. Astron. Soc.* **466**, 378–391 (2017).
41. Sotomayor-Beltran, C. et al. Calibrating high-precision Faraday rotation measurements for LOFAR and the next generation of low-frequency radio telescopes. *Astron. Astrophys.* **552**, A58 (2013).
42. Johnston, S. & Kerr, M. Polarimetry of 600 pulsars from observations at 1.4 GHz with the Parkes radio telescope. *Mon. Not. R. Astron. Soc.* **474**, 4629–4636 (2018).
43. Schnitzeler, D. H. F. M., Banfield, J. K. & Lee, K. J. Polarization signatures of unresolved radio sources. *Mon. Not. R. Astron. Soc.* **450**, 3579–3596 (2015).
44. Xu, J. & Han, J. L. Extragalactic dispersion measures of fast radio bursts. *Res. Astron. Astrophys.* **15**, 1629–1638 (2015).
45. Xu, J. & Han, J. L. Redshift evolution of extragalactic rotation measures. *Mon. Not. R. Astron. Soc.* **442**, 3329–3337 (2014).
46. Noutsos, A., Karastergiou, A., Kramer, M., Johnston, S. & Stappers, B. W. Phase-resolved Faraday rotation in pulsars. *Mon. Not. R. Astron. Soc.* **396**, 1559–1572 (2009).
47. Lu, W. & Kumar, P. On the radiation mechanism of repeating fast radio bursts. *Mon. Not. R. Astron. Soc.* **477**, 2470–2493 (2018).
48. Katz, J. I. Coherent emission in fast radio bursts. *Phys. Rev. D* **89**, 103009 (2014).
49. Waxman, E. On the origin of fast radio bursts (FRBs). *Astrophys. J.* **842**, 34 (2017).
50. Plotnikov, I. & Sironi, L. The synchrotron maser emission from relativistic shocks in Fast Radio Bursts: 1D PIC simulations of cold pair plasmas. *Mon. Not. R. Astron. Soc.* **485**, 3816–3833 (2019).
51. Sironi, L. & Spitkovsky, A. Acceleration of particles at the termination shock of a relativistic striped wind. *Astrophys. J.* **741**, 39 (2011).
52. Manchester, R. N. & Taylor, J. H. *Pulsars* (W. H. Freeman, 1977).
53. Cordes, J. M. & Chatterjee, S. Fast radio bursts: an extragalactic enigma. *Annu. Rev. Astron. Astrophys.* **57**, 417–465 (2019).
54. Zhang, B. Fast radio bursts from interacting binary neutron star systems. *Astrophys. J. Lett.* **890**, 24 (2020).
55. Zhang, Y. G. et al. Fast radio burst 121102 pulse detection and periodicity: a machine learning approach. *Astrophys. J.* **866**, 149 (2018).
56. Wang, W., Zhang, B., Chen, X. & Xu, R. On the time–frequency downward drifting of repeating fast radio bursts. *Astrophys. J. Lett.* **876**, 15 (2019).
57. Lyutikov, M. Radius-to-frequency mapping and FRB frequency drifts. *Astrophys. J.* **889**, 135 (2020).
58. Feroz, F., Hobson, M. P. & Bridges, M. MULTINEST: an efficient and robust Bayesian inference tool for cosmology and particle physics. *Mon. Not. R. Astron. Soc.* **398**, 1601–1614 (2009).

Acknowledgements This work used data from FAST, a Chinese national mega-science facility, built and operated by the National Astronomical Observatories, Chinese Academy of Sciences. This work is supported by the Natural Science Foundation of China (U15311243, 11988101, 11833009, 11690024, CAS XDB23010200), the Cultivation Project for FAST Scientific Payoff and Research Achievement of CAMS-CAS, the Max-Planck Partner Group, NKRDPIC 2017YFA0402600 and the Youth Innovation Promotion Association of CAS (2018075).

Author contributions R.L. led the observational proposal 2019a-129-P in the FAST ‘Shared-Risk’ observations and the statistical analysis of repeating events. B.J.W., Y.P.M., C.F.Z. and K.J.L. developed the searching pipeline and processed the raw data to produce FRB candidates. J.C.J. conducted the polarization calibration and RM measurements. H.X. conducted the flux calibration. R.N.C. and Y.J.G. performed the timing analysis. B.Z., W.Y.W., R.X.X. and J.P. provided theoretical discussions. J.Y., M.W. and N.W. contributed to discussions on observation planning. K.J.L., J.L.H. and B.Z. organized the FRB searching team, co-supervised the data analysis and interpretations and led the writing of the paper. The search software BEAR was tested by M.Z.C., X.L.C., L.F.H., Y.X.H., J.L., Z.X.L., J.T.L., X.P., Z.G.W. and Y.H.X. FAST observations, instrument setting and monitoring was done by P.J., L.Q., H.Q.G., H.L., J.H.S., J.Y., D.J.Y. and Y.Z. All authors contributed to the analysis or interpretation of the data and to the final version of the manuscript.

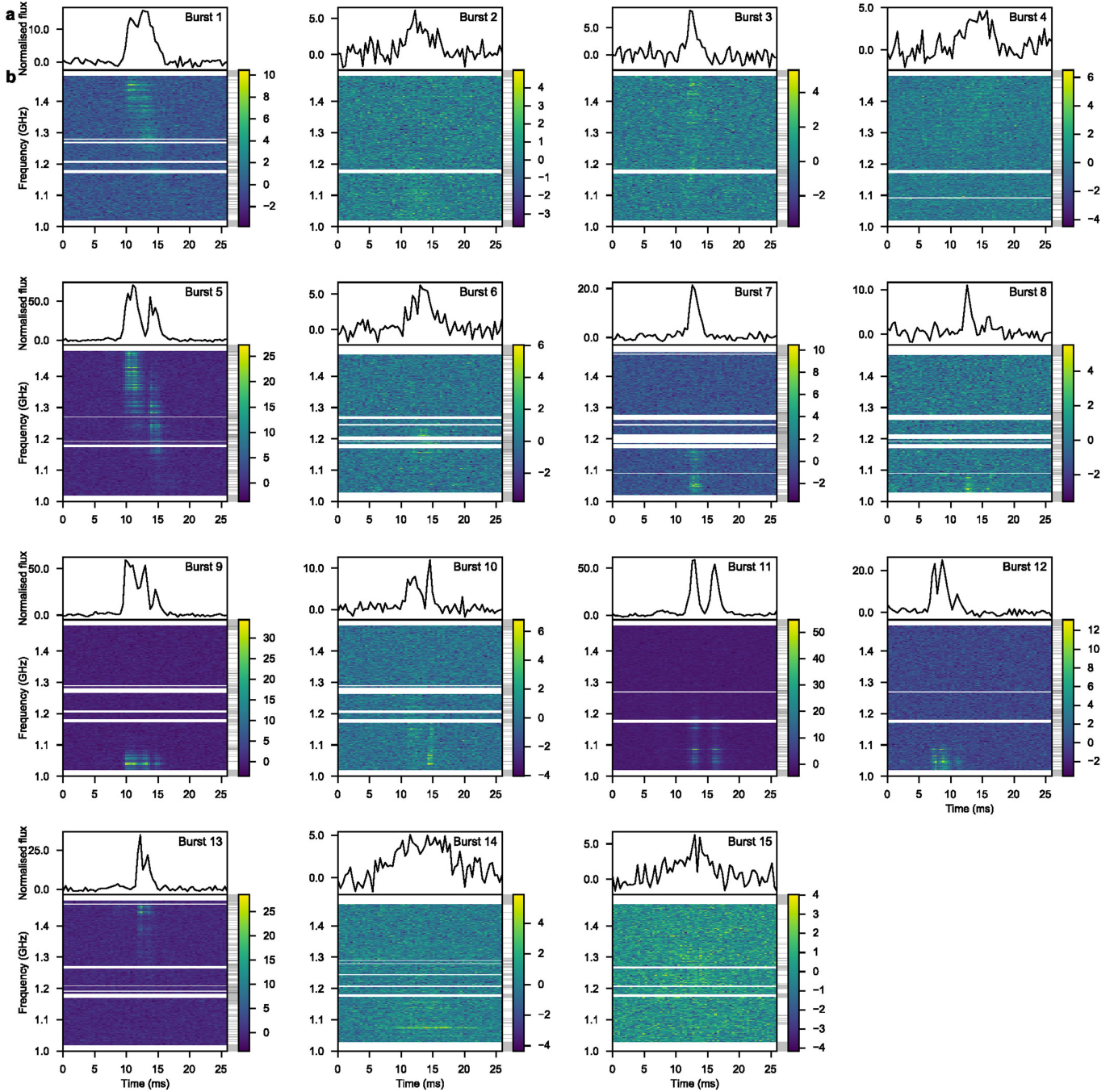
Competing interests The authors declare no competing interests.

Additional information

Correspondence and requests for materials should be addressed to K.J.L., J.L.H. or B.Z.

Peer review information *Nature* thanks Jason Hessels and Victoria Kaspi for their contribution to the peer review of this work.

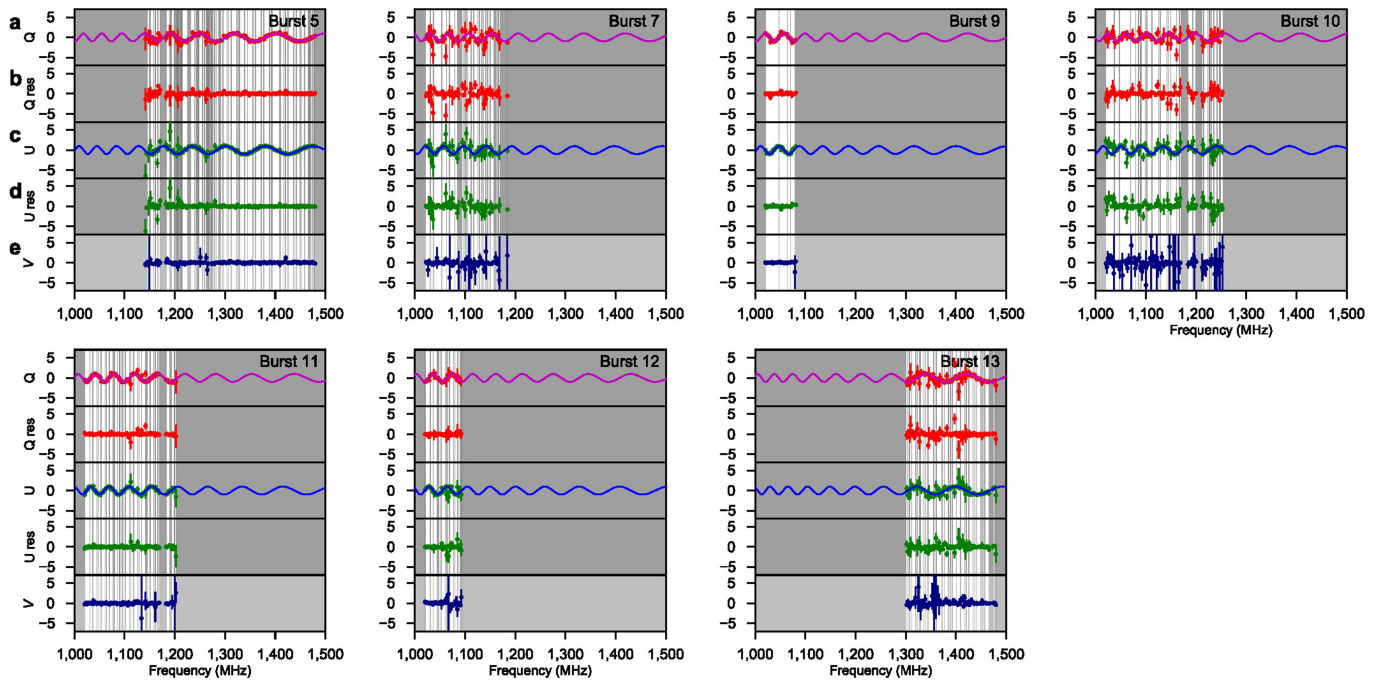
Reprints and permissions information is available at <http://www.nature.com/reprints>.



Extended Data Fig. 1 | Dynamic spectra for all 15 detected bursts of FRB 180301. a. Dedispersed pulse profile. **b.** Dynamic spectra for the total intensity as a function of frequency and time (with a frequency resolution 1.95 MHz per channel and a time resolution of 393.2 μ s per bin). The colour bars

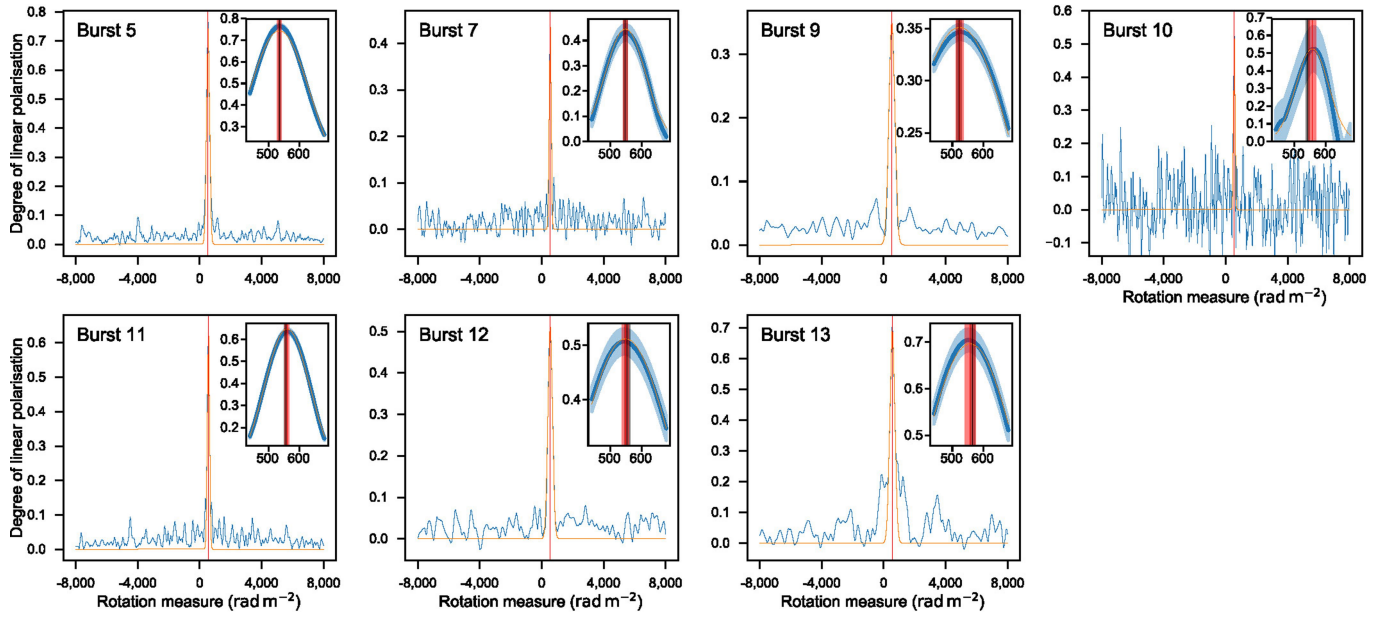
denote the intensity S/N scaled with the off-pulse r.m.s. value. The $DM_{aligned}$ values in Table 1 are used to dedisperse each burst. For bursts 1–4 we plot the raw intensity because only two linear polarization channels were recorded. For the rest of the bursts, polarization calibrations were performed.

Article



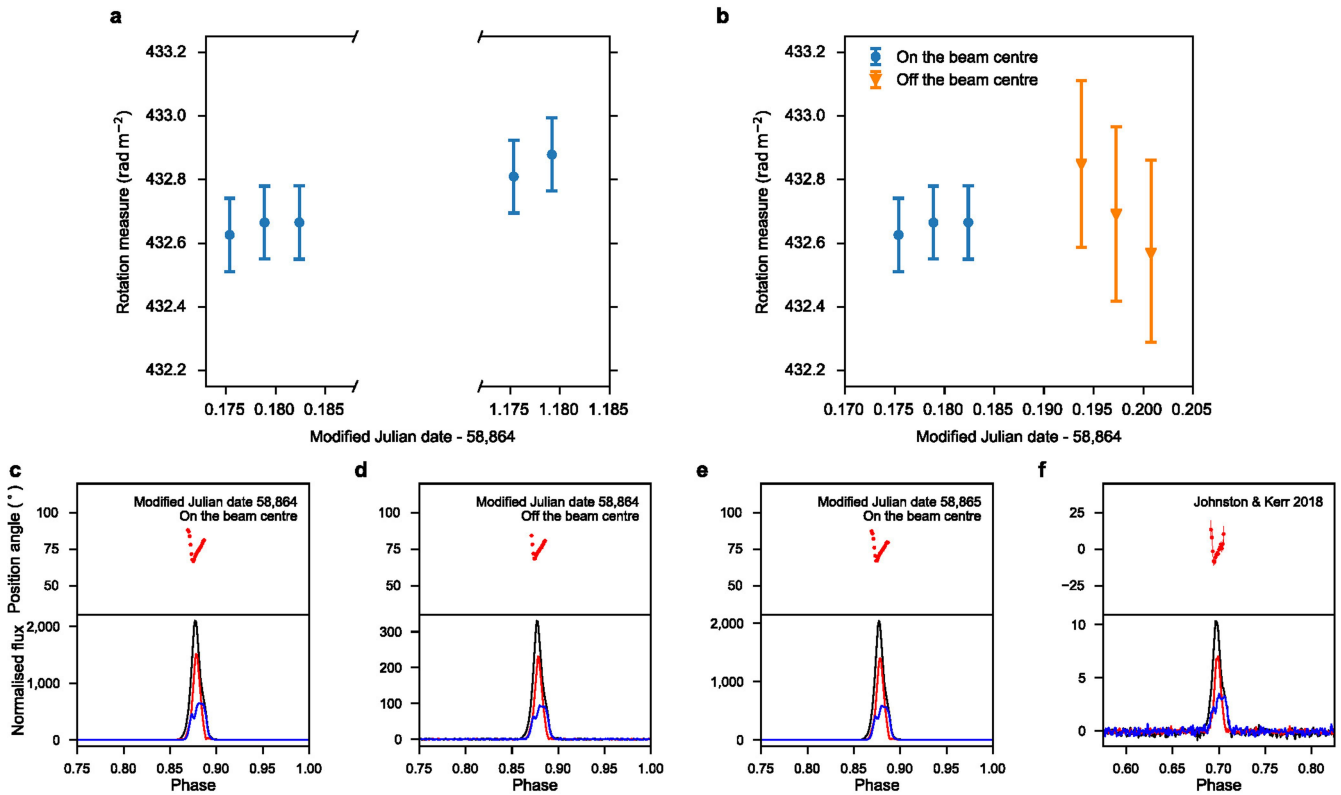
Extended Data Fig. 2 | Observed and fitted Stokes parameters Q and U for linear polarization as a function of frequency. **a, c, Normalized Stokes parameter Q and fitting residuals. **b, d,** Normalized Stokes parameter U and fitting residuals. The amplitudes of the oscillation have been normalized using the inferred linear polarization intensity. **e,** Stokes parameter V normalized by**

the total intensity in each channel. The grey shaded frequencies are removed before fitting owing to low signal intensities, RFI or band-edge effects. The error bars denote the 68% confidence intervals. The burst number in each subplot is as in Table 1.



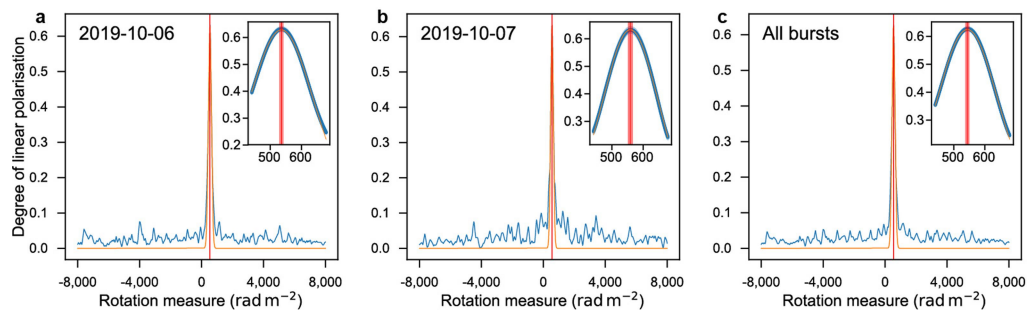
Extended Data Fig. 3 | RM synthesis results of the seven bursts. We calculate the RM spectrum within the range $-8,000$ to $+8,000$ rad m^{-2} . The horizontal red shaded area denotes the 1σ interval of the baseline. The vertical red line denotes the best-fit RM value. We also show a zoom-in of the spectral peak, where the vertical orange dashed lines show the range in which the spectrum is

used in peak fitting. The best-fitting Gaussian and its 68% confidence interval are indicated by the orange curve and blue shading. The vertical red lines and shading show the best-fit RM and the 68% confidence intervals. We also show the Bayesian RM, indicated by the vertical black lines and shading. The burst number in each sub-plot is defined in Table 1.

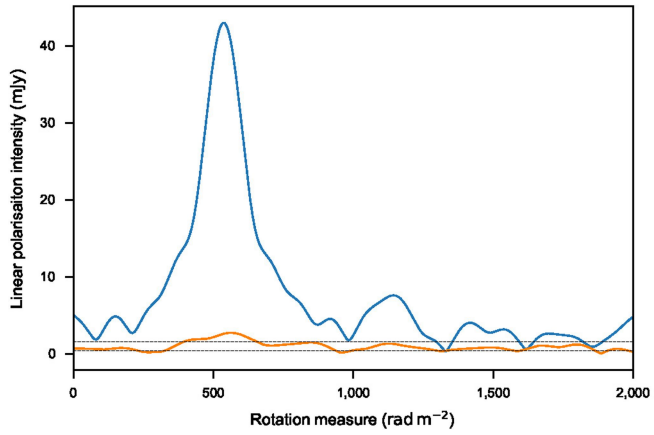


Extended Data Fig. 4 | Polarimetry stability test. a, Temporal stability test. The RM values of PSRJ1915+1009 measured with the Bayesian method confirm that there is no obvious RM variation in a one-day interval. The error bars denote 68% confidence intervals. **b**, Off-axis polarimetry test. PSRJ1915+1009 was first placed at the beam centre and then 2.6' away from the beam centre. The RM values measured with the Bayesian method confirm that there is no apparent systematic error for the off-axis illumination. The off-axis data point

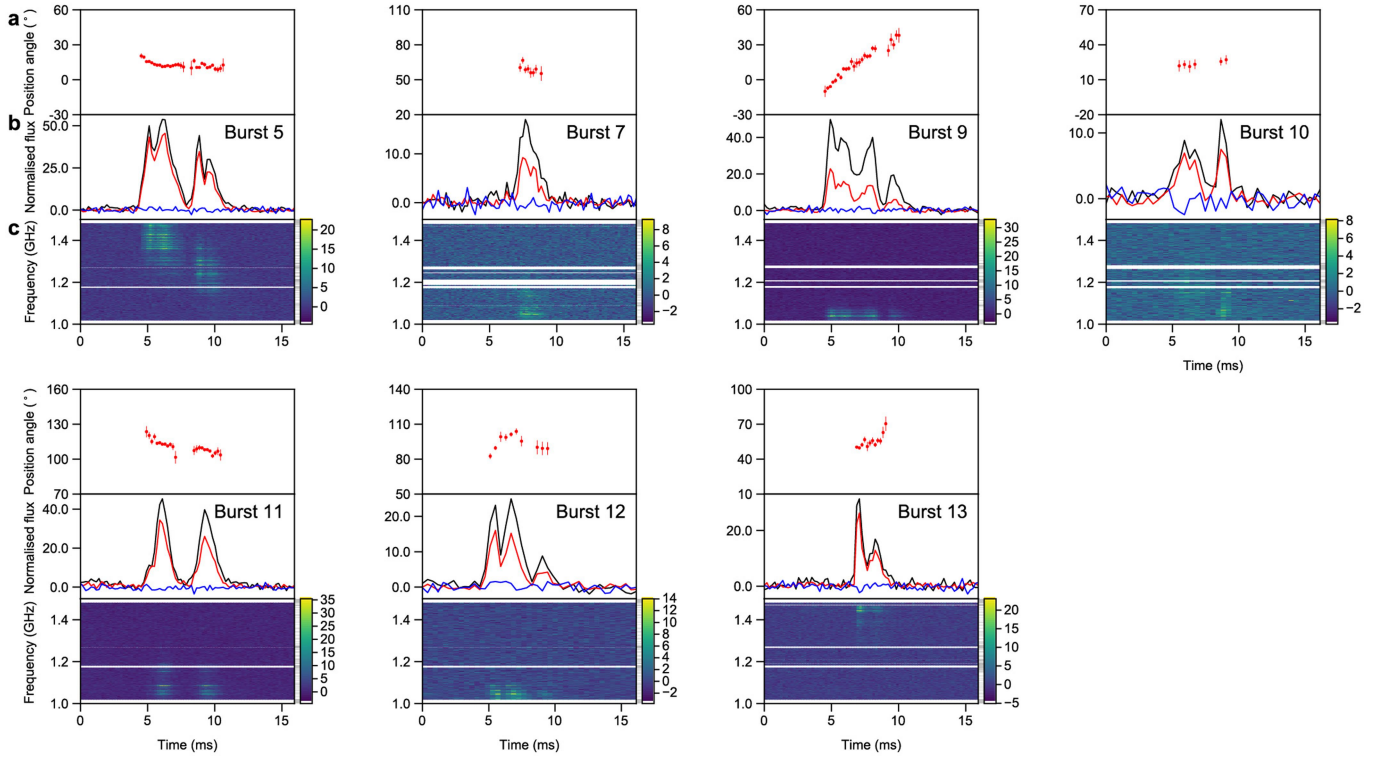
has a larger error because S/N drops for those observations owing to the off-axis illumination. **c**, Polarization pulse profile and PA for PSRJ1915+1009, observed with central illumination. **d**, As in **c**, but off-axis illumination is used. **e**, Polarization profile and PA with central illumination observed one day later. **f**, Polarization pulse profile measured with the Parkes radio telescope by Johnston & Kerr⁴².



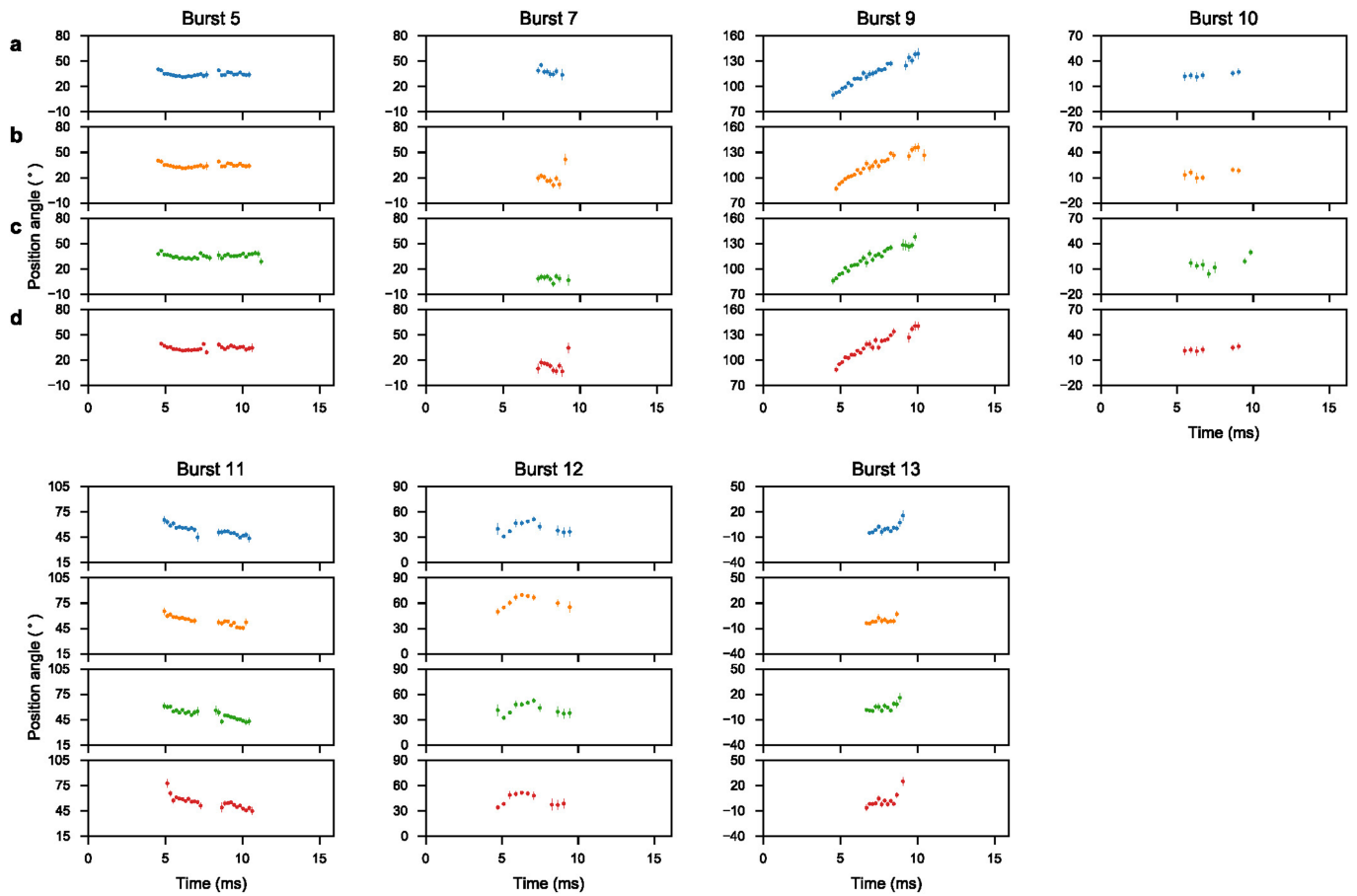
Extended Data Fig. 5 | The joint fitting results of the RM synthesis spectra. a, Bursts 5, 7, 9, 10 on 6 October 2019. **b**, Bursts 11, 12, 13 on 7 October 2019. **c**, All seven bursts. The notation is the same as in Extended Data Fig. 3.



Extended Data Fig. 6 | RM synthesis spectra before and after thin-screen subtraction. The blue and orange curve are the RM synthesis intensity spectra for burst 5. The orange curve is computed after subtracting the Stokes parameters Q and U corresponding to the RM of burst 5. The orange curve is consistent with noise. This indicates a thin-screen scenario for the Faraday rotation.

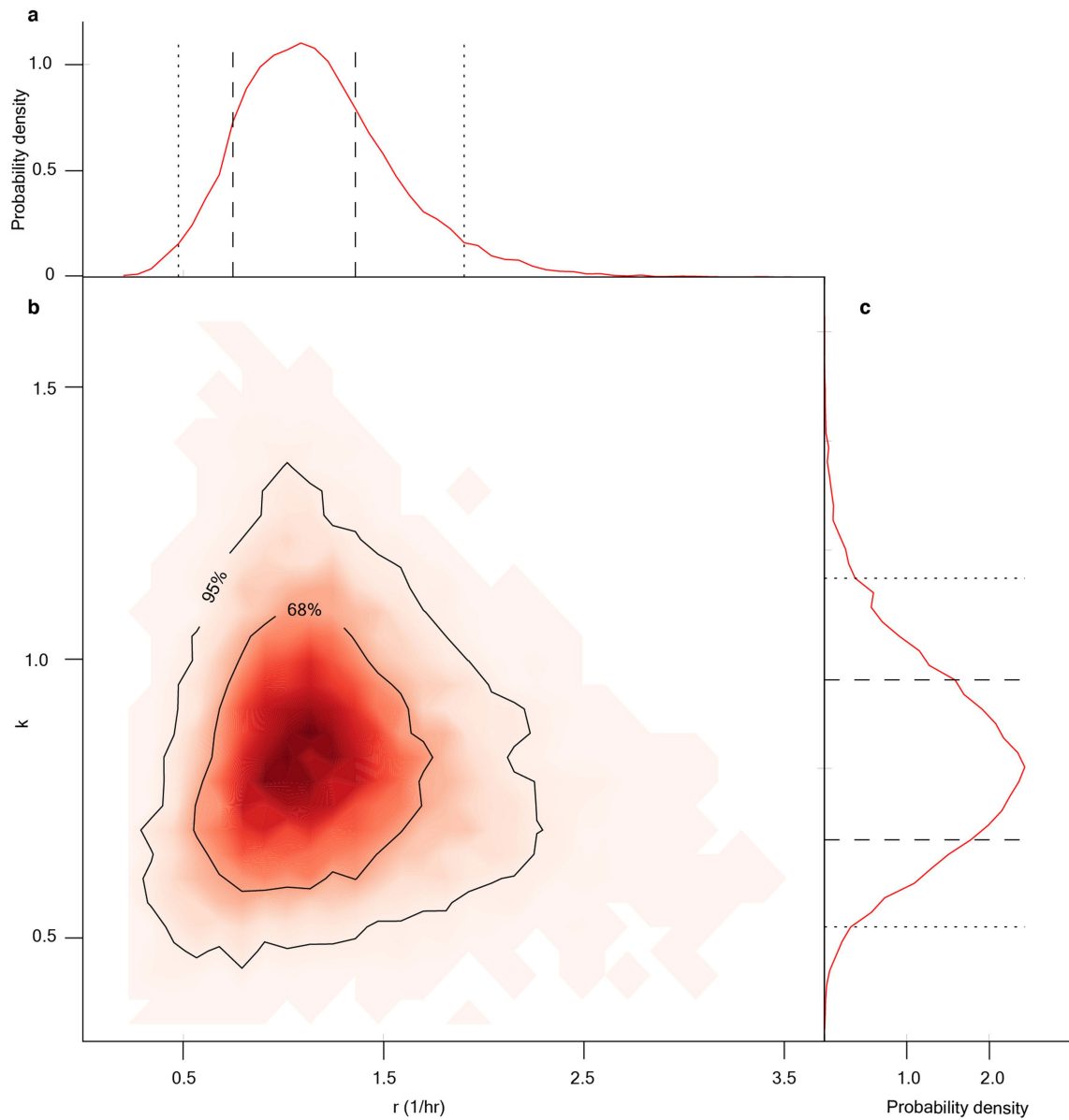


Extended Data Fig. 7 | Polarization profiles of seven bright bursts and their dynamic spectra. Here we used the globally fitted $RM = 543.7 \pm 2.6 \text{ rad m}^{-2}$ to derotate the linear polarization. The other settings are the same as in Fig. 1.



Extended Data Fig. 8 | Comparison of PA swing from seven bright bursts using different DM values in dedispersion. a–d. For each burst, blue curves use individually measured DM values as in Table 1 (a), orange curves use the DM

of burst 5 (b), green curves use the lowest DM (from burst 12) (c) and red curves use the highest DM (from burst 10) (d).



Extended Data Fig. 9 | Posterior distribution for the burst rate inference. **a**, Marginalized posterior of the burst rate. The dashed and dotted lines denote 68% and 95% confidence levels, respectively. **b**, Two-dimensional distribution

of the posterior. The horizontal and vertical axes show the burst rate and the shape parameter of the Weibull distribution, respectively. **c**, Marginalized posterior for the shape parameter.

Article

Extended Data Table 1 | FAST observations of FRB 180301

FAST observations of FRB 180301

Observational time UTC	MJD	Duration (hr:min)	Number of detections
2019-07-16 02:00:00 - 2019-07-16 04:00:00	58680	2:00	4
2019-09-11 21:52:00 - 2019-09-12 01:48:00	58737	3:56	0
2019-10-06 20:49:09 - 2019-10-06 23:49:09	58762	3:00	6
2019-10-07 20:33:23 - 2019-10-07 23:27:23	58763	2:56	5